**Key Points:**
- Globally, half of precipitation events are snow or come from melting snow
- Thirty percent of the precipitation events in the tropics come from melting snow
- This metric can be used to test other models

**Correspondence to:**
P. R. Field,
paul.field@metoffice.gov.uk

# Importance of snow to global precipitation

**P. R. Field[1,2] and A. J. Heymsfield[3]**

[1]Met Office, Exeter, UK, [2]Institute for Climate and Atmospheric Science, University of Leeds, Leeds, UK, [3]National Center for Atmospheric Research, Boulder, Colorado, USA

**Abstract** Precipitation controls the availability of drinking water and viability of the land to support agriculture. Failure to accurately predict the location, magnitude, and frequency of precipitation impacts not only numerical weather forecasting but also climate modeling. It has been proposed that most rainfall events originate from ice that has melted to form rain. Here we use remote sensing from spaceborne cloud radar to quantify that idea. A new metric is constructed to quantify the fraction of rain events at the surface that are linked to snow melting at a higher altitude. CloudSat is used to show the global variation of the importance of snow in the precipitation process. In the tropics, subtropics, midlatitude, polar regions, and globally 0.3, 0.4, 0.8, >0.9, and 0.5, respectively, of all precipitation events (>1 mm/d) are linked to the production of snow in clouds.

## 1. Introduction

Precipitation is an important component of the hydrological cycle. It has long been suggested that most rain is derived from ice that has melted to form rain [*Bergeron*, 1935]. Here we attempt to use remote sensing from spaceborne cloud radar to quantify that idea and make a comparison with a global model. It is clear that the warm rain process (no ice involved, which can occur at temperatures both above and below 0°C) can be dominant in the tropics and subtropics for shallow clouds. But how rapidly does the origin of rain transition from warm rain only to being intimately related to the evolution of the ice phase?

In a recent paper, *Mulmenstadt et al.* [2015] used CloudSat and CALIPSO data to produce a global climatology of precipitation frequency according to its thermodynamic phase whether solely through the liquid phase (warm rain), whether from snow aloft that melted to rain (cold rain) or entirely through the ice phase (snow). Phase was identified according to the properties at the top of the lowest cloud layer above precipitation onset in the column. This was done using a combination of the CloudSat cloud profiling radar and the lidar aboard CALIPSO that is incorporated into a radar-lidar combined data product. They found that the warm rain fraction is highest in the tropical and subtropical oceans outside of the Intertropical Convergence Zone (ITCZ), and cold rain dominates in the ITCZ over the midlatitude oceans and over continents. In this study we tackle a similar problem but differ from that work by introducing a new simply defined metric based on a fixed radar reflectivity threshold, make comparisons with ground sites, and compare to a global model.

In this study two questions are asked. First, if it is raining (greater than 1 mm/d) near the surface (1 km), then what fraction of those rain events came from melting snow? Second, if it is precipitating (rain or snow exceeding 1 mm/d) near the surface (1 km), then what fraction of those events are snow? CloudSat [*Stephens et al.*, 2008] spaceborne cloud radar observations are used to address these questions.

## 2. Methods
### 2.1. Constructing a New Precipitation Flag

To create the climatology presented in this study, a new precipitation flag has been generated from CloudSat, ground site, and model data (Figure 1a). For the satellite data we have chosen not to use CALIPSO lidar because it can only obtain useful data in regions that have an optical depth less than 3. Therefore, the lidar would not provide much additional data for many precipitating systems. Using reflectivity alone, a robust metric is produced that is independent of cloud type. The precipitation flag represents (0) no precipitation, (1) snow at the surface, (2) rain at the surface, and (3) rain at the surface contiguous with snow aloft in the same vertical column: rain from melting snow (rfms). These flags were generated for each CloudSat profile, model vertical
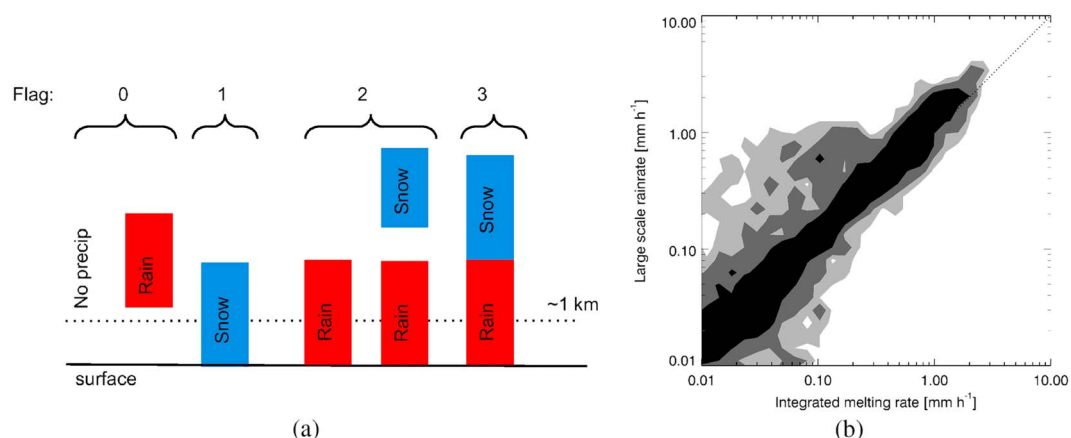
**Figure 1.** (a) Schematic showing the different hydrometeor profiles and the precipitation flag that would be assigned. (b) Joint histogram of rain rate at the surface compared to integrated melting rate of snow to rain in the column above obtained from model fields. Contour levels (darkest to lightest) contain 50, 75, and 95% of the data.

column, and ground site data. A threshold for CloudSat of 0 dBZ was chosen to detect precipitation events. Condensed water thresholds within the model were chosen that produced 0 dBZ assuming simple Rayleigh scattering based on the model particle size distributions and density assumptions. A reflectivity of 0 dBZ is equivalent to a precipitation rate of ~1 mm/d [e.g., *Matrosov*, 2007a].

## 2.2. CloudSat

The NASA CloudSat satellite has a 94 GHz, nadir-viewing cloud radar [*Stephens et al.*, 2008]. The spacecraft is in the A-train constellation of satellites that cross the equator at approximately 1.30 P.M. and A.M., local time. Three years (2008–2010) of CloudSat data have been used. We draw on the CloudSat radar 2B-GEOPROF and 2C-PRECIP products, the primary purpose of which is to identify those levels in the vertical column sampled by CloudSat that contain significant radar echo from hydrometeors and to provide a measure of the radar reflectivity factor for each of these volumes. The 2B-GEOPROF product [*Mace and Zhang*, 2014] provides information on the geographical location, the surface height bin information, radar signal, and a cloud mask flag that indicates the quality of the radar signal. The 2C-PRECIP product [*Haynes et al.*, 2009] is used to provide the freezing level height. The algorithm uses good quality CloudSat reflectivity data (cloud mask flag (2B-GEOPROF) 30–40) for ~1250 m and greater (range bin 5) above the surface to minimize the effects of ground clutter. These CloudSat data have been used to generate the four different precipitation flags introduced earlier. It is assumed that precipitation warmer than 0°C is liquid and ice if it is colder than 0°C. For each column, (i) if the reflectivity in the lowest used bin (fifth bin above surface) is less than the chosen threshold used to test for precipitation, then the flag is set to 0 (no precipitation). (ii) If this value exceeds the reflectivity threshold, and the freezing level is lower than this bin, then the flag is set to 1 (snow). (iii) If the reflectivity is greater than the threshold value and the freezing level is above the lowest bin used, then the flag is set to 2 (warm rain). (iv) If a flag of 2 is set, then a further test is carried out. If reflectivity values are found in two contiguous bins above the freezing level (0°C), then set flag to 3 (rain formed from melting snow), otherwise leave flag as 2 (warm rain process only).

Considerable attenuation is experienced by the 94 GHz signal due to dense ice particles and liquid water in convective clouds. Previous work has shown, through ground site and colocated spaceborne radar comparisons, that the CloudSat radar signal can be reduced by 10 dBZ or more [*Protat et al.*, 2009; *Sindhu and Bhat*, 2013]. Because the CloudSat radar reflectivity alone is unsuited to use as a direct estimate of precipitation rates in deep convective clouds, the formulation of methodologies that use the signal attenuation directly to estimate precipitation over the ocean [*Haynes et al.*, 2009] and also over the land [*Matrosov*, 2007b] has been developed. For this study we do not consider the precipitation rate but instead construct a metric that will be largely independent of the effects of attenuation. A threshold of 0 dBZ was chosen for use with CloudSat. Comparison of precipitation rates derived from an attenuation algorithm that is available over ocean only (2C-PRECIP [*Haynes et al.*, 2009]) and reflectivity at 1 km indicates that a reflectivity threshold of 0 dBZ corresponds to about 1 mm/d of precipitation. The use of this threshold means that many light drizzle events will be missed. Testing the sensitivity of the results to differences in reflectivity-precipitation rate

relations was assessed by changing the CloudSat precipitation threshold from 0 dBZ to −5 dBZ. This was found to make little difference to the results.

Generating the precipitation flag uses a very simple algorithm, and there are several potential issues. First, it is assumed that precipitation at 1 km will also be present at the surface. Model-based tests of this assumption indicate only slight changes to the results if the surface precipitation is used rather than the precipitation at 1 km to derive the precipitation flags. Second, the assumption that rain is contiguous with snow assumes that the rain has formed from the melting snow. This assumption was tested successfully in the model (see section 2.3). Third, precipitation particles above the freezing level are assumed to be ice. This assumption may not always be true but is likely to be satisfactory for most of the precipitation events that occur in regions with precipitation at subfreezing temperatures and where reflectivities are >0 dBZ. An advantage of such a simple algorithm is that it is less affected by retrieval assumptions and is amenable to including in models for comparison with the observations.

### 2.3. Global Model

As a demonstration of the utility of this analysis of the CloudSat data, the Met Office Unified Model was used to generate data for comparison to CloudSat observations. The Unified Model is used routinely for operational weather and climate prediction. It was run in a Numerical Weather Prediction mode with a midlatitude grid spacing of 25 km at midlatitudes. The model configuration used was GA6 (Global Atmosphere 6), which is essentially similar to the GA4 model configuration and parametrizations [*Walters et al.*, 2014], but with the introduction of an updated semi-Lagrangian dynamical core [*Wood et al.*, 2014].

The algorithm for constructing the precipitation flags for the model uses instantaneous values and is the same as that used for CloudSat. The only difference is that a condensed water content threshold consistent with the 0 dBZ radar reflectivity threshold was used for analyzing the model data. Flags have been computed based on a level about 1 km above the surface over ocean. The impact of assumptions about the particle size distributions, density, and the subgrid distribution of condensed water content will be explored in later papers.

An underlying assumption in our analysis is that if snow is contiguous with rain in a vertical column, then the rain is formed from the melting snow. To test this assumption, the model-derived snow melting rate on each level in the vertical was multiplied by the model layer thickness and summed to provide the column-integrated melting rate. This was plotted against the surface rain rate for model columns with flag 3. If no other processes, such as evaporation and accretion, are acting, then this plot should be 1:1 for steady state conditions. Because the model uses a prognostic representation for hydrometeors, temporal variations in the microphysical column will contribute to some variation in this plot. This is due to rain at the surface being linked to melting carried out at earlier model time steps. Figure 1b shows that the column-integrated melting rate of snow is a good predictor of the rain rate at the surface. This physical link supports our assertion that columns with flag set to 3 for CloudSat are indicating regions where the rain at the surface is formed from melting snow aloft.

For the model, 10 day runs initialized from the first of each month of one of the years used in the CloudSat analysis (2010) have been carried out to construct an annual sample consisting of 120 days spaced throughout the year. The instantaneous data are output at 0, 6, 12, and 18 UTC hours. The data are regridded onto a 4° latitude-longitude grid.

### 2.4. Ground Sites

One year (2008) of ARM (Atmospheric Radiation Measurement Program) [*Stokes and Schwartz*, 1994] data from the North Slope of Alaska (NSA), Southern Great Plains (SGP), and Tropical West Pacific (TWP) sites were analyzed to compare with the satellite data. Because the ARM site radar is looking up, when there is liquid precipitation, there is significant attenuation of the radar reflectivity signal and so MICROBASE radar cloud retrieval products [*Dunn et al.*, 2011] for phase and condensed water amounts were used. These MICROBASE retrievals were rebinned from the original time and vertical resolution (5 s, 45 m) into 225 m and 5 min meaned values to approximate the CloudSat data resolution (250 m vertical, 2 km footprint, assuming 7 m s$^{-1}$ horizontal wind for 5 min). Thresholds of 0.1 g m$^{-3}$ for liquid and ice water content to equate to the 0 dBZ reflectivity threshold used for the CloudSat analysis were used. The ice water content threshold was based on the *Liu and Illingworth* [2000] reflectivity-ice water content relation used for the MICROBASE retrieval. For cases where precipitation was present, a threshold of 0.001 g m$^{-3}$ was used to determine if snow was above the liquid. Each profile was inspected at a low level (~1200 m) to determine if precipitation was occurring. If the liquid

water threshold was exceeded, a flag of 2 was assigned. If the ice water content threshold was exceeded, then a flag of 1 was assigned. For profiles assigned with flag = 2 the profile was inspected to determine if ice water content exceeding the 0.001 g m$^{-3}$ ice threshold was lying on top of the liquid water. If this was the case, then a flag of 3 was assigned to that profile.

Surface estimates for $F_s$ were obtained from Global Historical Climatology Network daily data [*Menne et al.*, 2012] for 2008. Sites that reported the same number of snow and liquid precipitation reports for 80% of that year were used. To thin the data over North America, only the first site where the first five letters of the station name are the same were used. If any snow accumulation was recorded, then the flag was set to 1. If liquid precipitation was recorded, the flag was set to 2. The three ARM sites NSA, SGP, and TWP were also used to estimate $F_s$ using the threshold discussed above.

## 3. Fraction of Precipitation Events Linked to Snow

Using the precipitation flags described above, the fraction of rain events from melting snow and precipitation events that are snow were computed as follows.

Fraction of rain events formed from melting snow:

$$F_{rfms} = \frac{n_3}{n_2 + n_3} \tag{1}$$

Fraction of precipitation events that are snow:

$$F_s = \frac{n_1}{n_1 + n_2 + n_3} \tag{2}$$

where $n_{1,2,3}$ are the number of samples in each 4° grid box with flag 1, 2, or 3. Fractions are only computed if 10 or more events ($n_3 > 9$ for $F_{rfms}$ or $n_2 > 9$ for $F_s$) are detected. Poisson statistics indicate standard deviations within 0.1 only rising to 0.2–0.3 near to the Sahara and close to the Antarctic continent.

Figure 2a shows the global map of the annual fraction of rain events at 1 km altitude greater than 0 dBZ from CloudSat formed from the melting of snow above ($F_{rfms}$). It shows generally greater values toward the poles and over land. The 1-$F_{rfms}$ gives the warm rain only fraction. It can be seen that the subtropical stratocumulus regions are dominated by the warm rain process as expected. Fractions of rain from snow events are greater than 0.5 for North America to the east of the Rockies. The 0.5 contour then tracks northeastward along the North Atlantic storm tracks where it crosses Northern Europe and stays to the north side of the Himalayas and the northern borders of China before following the North Pacific storm track back toward North America. In the Southern Ocean the 0.5 contour has less latitudinal variation and is located at about 50°S. South America, Africa, Southeast Asia, and Australasia land areas are generally dominated by fractions exceeding 0.4. The Atlantic portion of the Intertropical Convergence Zone (ITCZ), the Maritime Continent, and the ITCZ just off the west coast of Mexico all exhibit fractions of rain formed from melting snow of greater than 0.4.

The annual fraction of precipitation events that are snow where the precipitation rate at 1 km is greater than 0 dBZ is given in Figure 2b. In the Southern hemisphere there is a steady increase of the snow fraction toward the pole as is to be expected. The only interruption to this uniform behavior occurs over the Andes where fractions of snow events exceeding 0.1 reach almost to the equator. In the Northern Hemisphere, the gradual increase in snow fraction toward the pole is modulated by the land and orographic features. The dominance of snow events can be seen clearly over the Himalayas and the Urals where the latter deflects the fraction of occurrence of snow equatorward toward the Caspian Sea.

Seasonal maps are given in Figure 3. For $F_{rfms}$ the summer hemisphere is very similar to the annual mean. In the winter hemisphere, where the precipitation is not dominated by snow, the $F_{frms}$ contours migrate farther equatorward than for the summer, while over the tropics the band of higher $F_{frms}$ follows the migration of the ITCZ. The seasonal plots indicate that the Northern Hemisphere with its greater land fraction experiences a much larger variation of $F_s$ than the Southern Hemisphere.

Figure 4 shows the same fractions as Figure 2 but derived from the model. The model and observations indicate that the gross temperature and cloud structures in the model have some similarity, but spatial variability and the magnitude of the $F_{rfms}$ metric can differ considerably between the model and observations.
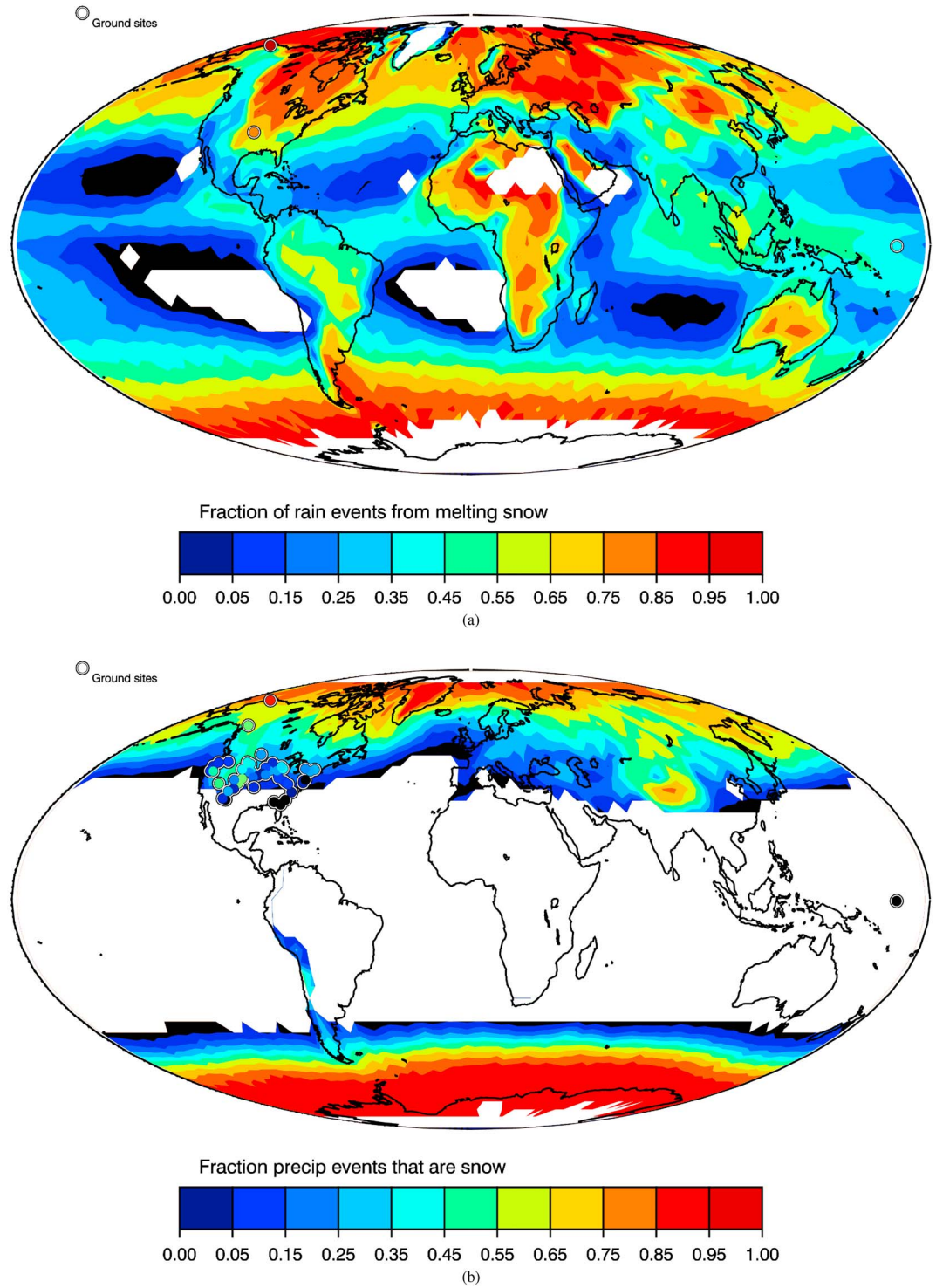
**Figure 2.** (a) CloudSat derived annual fraction of rain events at the 1 km (reflectivities > 0 dBZ) formed from melting snow above. (b) CloudSat-derived annual fraction of snow events at the ~1 km for reflectivities > 0 dBZ. White areas indicate regions with too few precipitation events above the 0 dBZ threshold. Circles represent ground-based observations from ARM sites only in Figure 2a while both ARM site and GHCN station data are depicted in Figure 2b.
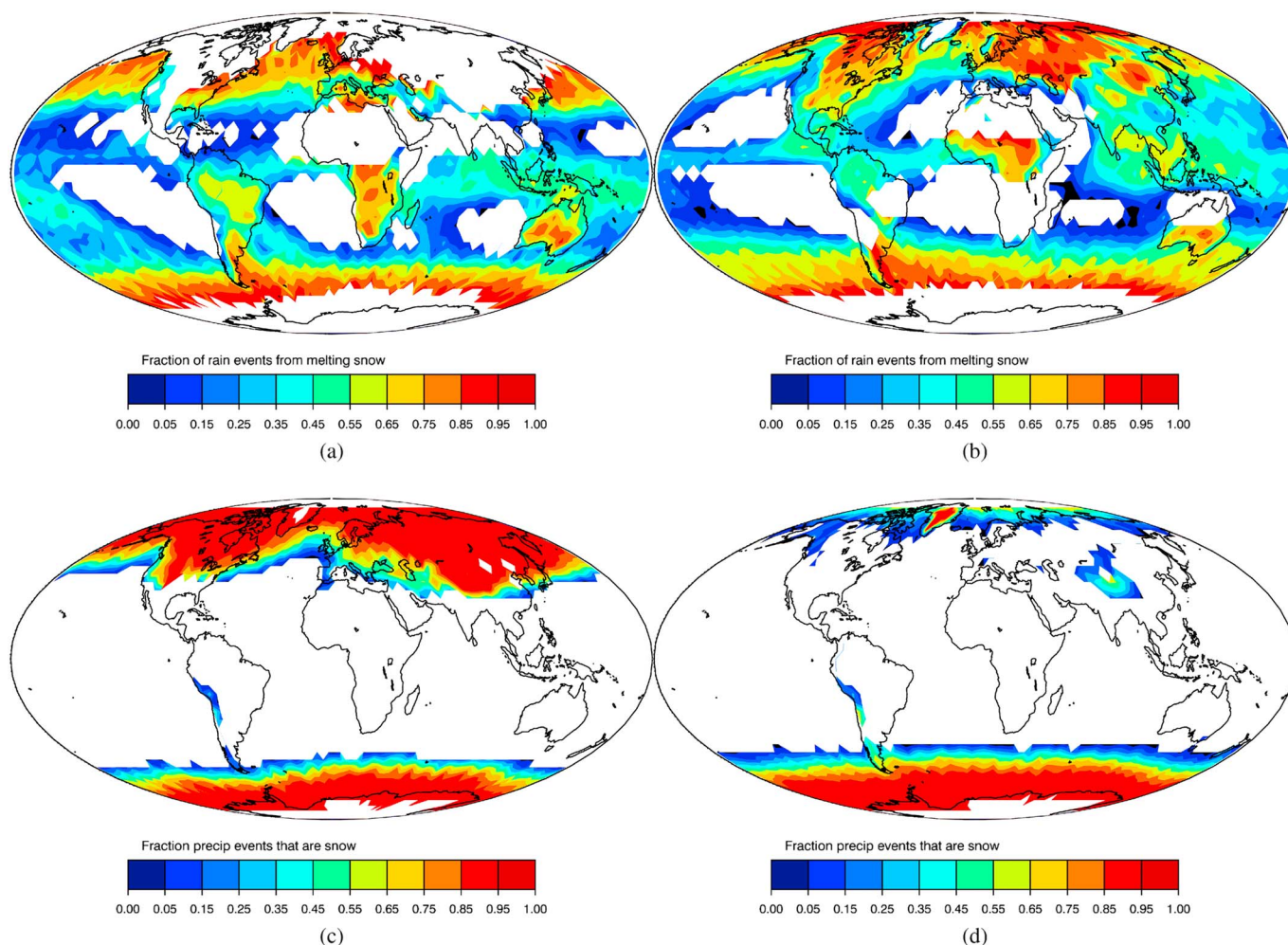
**Figure 3.** Same as Figure 2 but for season (a and c) December, January, and February and (b and d) June, July, and August.

Patterns of $F_s$ are very similar to previous snow climatologies [*Liu*, 2008], picking out a snow signal along the Andes and Himalayas extending to relatively low latitudes, but in this study the fractions are greater because of the conditional sampling on the presence of precipitation. Although the equatorward edge of $F_s$ is similar for both model and Cloudsat as depicted by the 0.1 contour, the model $F_s$ values decrease over a much smaller latitude range than Cloudsat. For example, the $F_s = 0.5$ contour is generally farther equatorward in the model Northern Hemisphere when compared to Cloudsat. For $F_{rfms}$, the model values are up to $\sim 0.2$ lower than the observations and there are spatial differences, most notably across the Rockies and onto central and eastern North America and a band running across Southern Europe into Asia. These differences indicate that improvements need to be made to the model to capture the behavior of these metrics better.

Ground site comparisons of the three ARM sites for $F_{rfms}$ (NSA: 0.9, SGP: 0.7, and TWP: 0.3) show good agreement with the satellite estimates. Reducing the ice water content threshold for determining flag 3 in the ARM site analysis by a factor of 10 increases the ARM site $F_{rfms}$ by $\sim 0.05$: less than one contour interval. Increasing the threshold by a factor of 10 is more significant decreasing the $F_{rfms}$ values by $\sim 0.2$. The ground sites allow the analysis to assess the effect of using near-surface values of condensed water to determine whether precipitation is occurring. Using a height of $\sim 300$ m instead of $\sim 1200$ m results in slight (0.05) reductions of $F_{rfms}$ for the SGP and TWP sites but a larger reduction of $\sim 0.3$ for the NSA.

The ground site estimates of $F_s$ broadly capture the spatial variability and magnitude of the values derived from CloudSat, exhibiting relatively greater values over the Rockies.
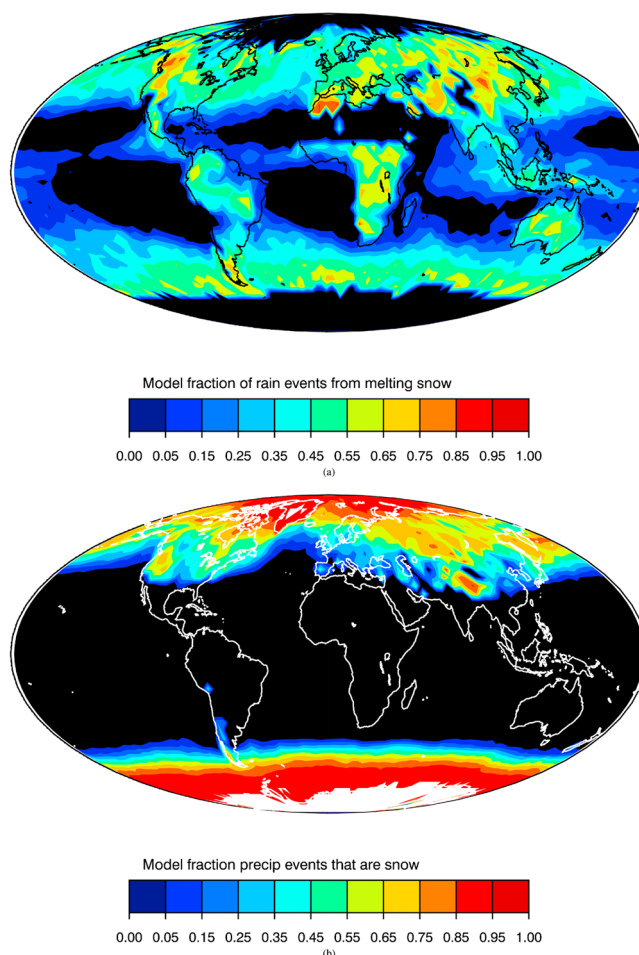
**Figure 4.** Same as Figure 2 but for the model.

## 4. Discussion and Summary

The initial comparison between the model and the CloudSat observations indicates that this is a promising way to assess the microphysical fidelity of global models and investigate the role of snow in a changing climate. Future work will investigate the sensitivity of this climatology to cloud microphysical processes such as ice nucleation and other important parametrizations for cloud such as the convective cloud and cloud fraction representations.

The results presented here are generally in agreement with *Mulmenstadt et al.* [2015] but differ in some continental regions such as the Rockies and over Europe. For instance, the frequency of occurrence of warm rain over land is almost absent in the Mulmenstadt et al. study, whereas we see values greater than 0.1 with spatial variations in this value (1-$F_{rfms}$; see Figure 1a). The reasons for the differences between these studies will be explored in future work. We note that the pattern of $F_{rfms}$ over the Rockies from CloudSat presented in this work (Figure 2a) can be seen in other observational-based climatologies. For example, a climatology of precipitation associated with midlatitude cyclones [*Hawcroft et al.*, 2012] shows much greater values to the east of the Rockies rather than over the Rockies themselves. For Europe the CloudSat-derived $F_{rfms}$ pattern is also similar to that seen for precipitation associated with midlatitude cyclones. Similarly, lightning climatologies [*Cecil et al.*, 2014] also show relatively lower values of flash rate over the Rockies when compared to the continental region to the east. And over Central Asia there is a belt of relatively lower lightning flash rate that is suggestive of reduced levels of deep convection. The agreement between the spatial patterns exhibited by the lightning climatology, the midlatitude precipitation climatology, and this climatology makes physical sense if it is accepted that these phenomena indicate where deep precipitation clouds that span the freezing level are present.

**Table 1.** Averaged Values for the Fraction of Rain Events at 1 km That Are Derived From Melting Snow and the Fraction of Precipitation Events at 1 km That Are Snow[a]

| | $F_{rfms}$: Annual fraction of rain events from melting snow. All points (land only, sea only) | | $F_s$: Annual fraction of precipitation events that are snow. All points (land only, sea only) | | Annual fraction of precipitation events linked to snow $F_{s+rfms} = \frac{n_1+n_3}{n_1+n_2+n_3}$ | |
|---|---|---|---|---|---|---|
| | CloudSat | Model | CloudSat | Model | CloudSat | Model |
| Tropics [0.36] | | | | | | |
| (0°–23.5°) | 0.34 (0.45, 0.29) | 0.14 (0.41, 0.11) | 0.00 (0.00, 0.0) | 0.00 (0.01, 0.00) | 0.34 | 0.14 |
| Subtropics [0.38] | | | | | | |
| (23.5°–38°) | 0.35 (0.43, 0.33) | 0.27 (0.46, 0.24) | 0.07 (0.15, 0.00) | 0.03 (0.13, 0.01) | 0.40 | 0.29 |
| Midlatitudes [0.40] | | | | | | |
| (38°–66.5°) | 0.71 (0.67, 0.73) | 0.53 (0.57, 0.51) | 0.49 (0.51, 0.44) | 0.51 (0.54, 0.49) | 0.85 | 0.77 |
| Polar [0.71] | | | | | | |
| (66.5°–90°) | 0.83 (0.76, 0.91) | 0.48 (0.42, 0.48) | 0.90 (0.90, 0.86) | 0.88 (0.88, 0.88) | 0.98 | 0.94 |

[a]The last two columns combine $F_{rfms}$ and $F_s$ to obtain the fraction of precipitation that is associated with the ice phase. The values in brackets are for land-only and sea-only points, respectively. In the first column the number in square brackets is the land fraction in each latitude range.

A summary of results over different latitudinal ranges (Table 1) indicates the expected increase in the fraction of precipitation events linked to snow with increasing latitudinal zone. The small fraction of snow events for the subtropics is due to the presence of high orography at these latitudes. For $F_{rfms}$, the model exhibits lower fractions than the observations, while for $F_s$ the model exhibits similar values to do observations. Dividing the results into land- and sea-only points within each climatological band indicates that high $F_{rfms}$ occur largely over land masses in the tropics and subtropics, consistent with lightning data that suggest that vigorous, lightning-produced convection over land areas. From the observations, in the subtropics a third to a half of the precipitation events are related to the ice phase. In the midlatitudes the majority of the precipitation events is linked to the ice phase and the rain from melting snow accounts for greater than two thirds of rain events. Globally, from CloudSat, the area-averaged fraction of rain events related to melting snow is 0.48. These results quantifiably demonstrate that the accurate representation of the evolution of the ice phase is of great importance to the prediction of rain at the surface over much of the globe.

**References**

Bergeron, T. (1935), On the physics of clouds and precipitation, in *Proces Verbaux de l'Association de Meteorologie*, pp. 156–178, Intl. Union of Geod. and Geophys., Paris.

Cecil, D. J., D. E. Buechler, and R. J. Blakeslee (2014), Gridded lightning climatology from TRMM-LIS and OTD: Dataset description, *Atmos. Res.*, 135-136, 404–414.

Dunn, M., K. L. Johnson, and M. P. Jensen (2011), The MICROBASE value-added product: A baseline retrieval of cloud microphysical properties, DOE/SC-ARM/TR-095. [Available at http://www.arm.gov/publications/techreports/ doe-sc-arm-tr-095.pdf.]

Hawcroft, M. K., L. C. Shaffrey, K. I. Hodges, and H. F. Dacre (2012), How much Northern Hemisphere precipitation is associated with extratropical cyclones?, *Geophys. Res. Lett.*, 39, L24809, doi:10.1029/2012GL053866.

Haynes, J. M., T. S. L'Ecuyer, G. L. Stephens, S. D. Miller, C. Mitrescu, N. B. Wood, and S. Tanelli (2009), Rainfall retrieval over the ocean with spaceborne W-band radar, *J. Geophys. Res.*, 114, D00A22, doi:10.1029/2008JD009973.

Liu, G. (2008), Deriving snow cloud characteristics from CloudSat observations, *J. Geophys. Res.*, 113, D00A09, doi:10.1029/2007JD009766.

Liu, C.-L., and A. J. Illingworth (2000), Toward more accurate retrievals of ice water content from radar measurements of clouds, *J. Appl. Meteorol.*, 39, 1130–1146.

Mace, G. G., and Q. Zhang (2014), The CloudSat radar-lidar geometrical profile product (RL-GeoProf): Updates, improvements, and selected results, *J. Geophys. Res. Atmos.*, 119, 9441–9462, doi:10.1002/2013JD021374.

Matrosov, S. Y. (2007a), Potential for attenuation-based estimations of rainfall rate from CloudSat, *Geophys. Res. Lett.*, 34, L05817, doi:10.1029/2006GL029161.

Matrosov, S. Y. (2007b), Modeling backscatter properties of snowfall at millimeter wavelengths, *J. Atmos. Sci.*, 64, 1727–1736.

Menne, M. J., I. Durre, R. S. Vose, B. E. Gleason, and T. G. Houston (2012), An overview of the Global Historical Climatology Network daily database, *J. Atmos. Oceanic Technol.*, 29, 897–910, doi:10.1175/JTECH-D-11-00103.1.

Mulmenstadt, J., O. Sourdeval, J. Delanoe, and J. Quaas (2015), Frequency of occurrence of rain from liquid-, mixed-and ice-phase clouds derived from A-Train satellite retrievals, *Geophys. Res. Lett.*, 42, doi:10.1002/2015GL064604.

Protat, A., D. Bouniol, J. Delanoe, E. O'Connor, P. T. May, A. Plana-Fattori, A. Hasson, U. Garsdorf, and A. J. Heymsfield (2009), Assessment of CloudSat reflectivity measurements and ice cloud properties using ground-based and airborne cloud radar observations, *J. Atmos. Oceanic Technol.*, 26, 1717–1741.

Sindhu, K. D., and G. S. Bhat (2013), Comparison of CloudSat and TRMM radar reflectivities, *J. Earth Syst. Sci.*, 122, 947–956.

Stephens, G. L., et al. (2008), CloudSat mission: Performance and early science after the first year of operation, *J. Geophys. Res.*, 113, D00A18, doi:10.1029/2008JD009982.

Stokes, G. M., and S. E. Schwartz (1994), The Atmospheric Radiation Measurement (ARM) program: Programmatic background and design of the cloud and radiation test bed, *Bull. Am. Meteorol. Soc.*, 75, 1201–1221.

Walters, D. N., et al. (2014), The Met Office Unified Model Global Atmosphere 4.0 and JULES Global Land 4.0 configurations, *Geosci. Model Dev.*, *7*, 361–386, doi:10.5194/gmd-7-361-2014.

Wood, N., et al. (2014), An inherently mass-conserving semi-implicit semi-Lagrangian discretisation of the deep-atmosphere global nonhydrostatic equations, *Q. J. R. Meteorol. Soc.*, *140*, 1505–1520, doi:10.1002/qj.2235.